Ultrafast All-Optical Reversible Peres and Feynman-Double Logic Gates with Silicon Microring Resonators

Purnima Sethi and Sukhdev Roy(✉)

Department of Physics and Computer Science, Dayalbagh Educational Institute, Dayalbagh, Agra 282 005, India
sukhdevroy@dei.ac.in

Abstract. We present designs of reversible Peres logic gate and Feynman-Double logic gate based on all-optical switching by two-photon absorption induced free-carrier injection in silicon add-drop microring resonators. The logic gates have been theoretically analyzed using time-domain coupled-mode theory and all-optical switching has been optimized for low-power (25 mW) ultrafast (25 ps) operation with high modulation depth (85 %) to enable logic operations at 40 Gb/s. The advantages of high Q-factor, tunability, compactness, cascadibility, reversibility and reconfigurability make the designs favorable for practical applications.

Keywords: All-optical switching · Optical computing · Microring resonator · Directed logic · Reversible logic · Silicon photonics

1 Introduction

Silicon photonics has emerged as the most promising platform to achieve the next generation ultrafast and ultrahigh bandwidth communication and computing. It exploits the advantages of optics i.e. parallelism, ultrahigh speed and bandwidth along with CMOS compatibility to deliver ultra-compact energy-efficient circuits, thus enabling dense integration with current microelectronics [1–4]. Photonic integrated circuits on silicon-on-insulator platform increases yield and reliability, allows for large volume manufacturing at low cost and offer reduction in size, weight and power consumption [5]. However, power optimization along with faster computing is a major technological challenge that requires new computing paradigms [6–13]. Directed Logic (DL) and Binary Decision Diagram (BDD) are newly proposed strategies which minimize the latency in calculating a complicated logic function by taking advantage of fast and low-loss propagation of light in a highly integrated on-chip photonic system [6–9].

Conventional classical computing is based on Boolean logic that is irreversible, that is, the inputs cannot be inferred from the output, as the number of output bits is less than the inputs. This leads to destruction of information and hence to the dissipation of a large amount of energy. This limitation can be overcome by conservative and reversible logic that circumvents information loss and opens up the possibility of ultra-low power computing [10–18].

© Springer-Verlag Berlin Heidelberg 2014
M.L. Gavrilova et al. (Eds.): Trans. on Comput. Sci. XXIV, LNCS 8911, pp. 21–36, 2014.
DOI: 10.1007/978-3-662-45711-5_2

Reversible computing is motivated by the von Neumann-Landauer (VNL) principle, according to which ordinary irreversible logic operations which destructively overwrite previous outputs incur a fundamental minimum energy cost [11]. According to Landauer, in order for a computational process to be physically reversible, it must also be logically reversible. Reversible logic is also quintessential to enable revolutionary optical and quantum computing paradigms. Quantum arithmetic is built from reversible logical components, as unitary operations are reversible [15, 16].

A switch is the fundamental building block of computing circuits. Advances in the fabrication of micro and nanostructures have opened up exciting possibilities to generate, modulate and detect light to achieve energy efficient optical supercomputing and communication [5, 6]. Silicon microring resonators (MRRs) provide an excellent platform for optical switching and computing offering high-Q, ultrafast switching, ultralow-power consumption, ease of fabrication, large scale integration and versatility [19, 20]. Silicon MRRs based optical switches modulated by electrical, thermal, or optical signals have been widely investigated [6–9, 21–25]. Modulation with MRRs is advantageous as they are compact, can be actuated directly as a lumped element and their relatively small area limits the necessary power to modulate, making them hold the best potential in terms of modulation energy per bit [20]. Recently, an experimental demonstration of fast all-optical switching using silicon MRRs has been shown [21]. The transmission of the structure can be modulated by up to 94 % in less than 500 ps using light pulses with energies as low as 25 pJ [21].

All-optical switching in silicon MRRs based on free-carrier injection by two-photon absorption (TPA) has been experimentally shown in all-pass (1 × 1) and add-drop (1 × 2) configurations [21–25]. All-optical AND/NAND and half-adder/full-adder circuits have been realized using 1 × 1 MRRs only [9, 23]. Although electro/thermo-optic implementations of various logic circuits with switching speed of ∼ns–ms and bit rate 100–10 kbit/s have been shown using arrays of silicon MRRs, they suffer from lower switching response and bit rates [6–9]. Reduction in the number of switches can substantially reduce power consumption, delay, latency and size of devices. Caulfield and Soref have proposed a reconfigurable electro-optical system with SOI resonant structures using dual MRRs [26]. Although, the circuits facilitate unidirectional signal propagation for cascadability, they require relatively more switches, besides adding complexity due to the dual ring structure. BDD/DL based all-optical computing with silicon MRRs therefore, holds the best potential for high-bandwidth, high-density, low-power devices that can viably be inserted within the chip packaging solution. All-optical logic is essential to avoid optoelectronic conversions, which constrain broadband, high speed and flexible systems. DL based reversible and reconfigurable all-optical logic using silicon MRRs is therefore extremely important for realization of low-cost, ultrafast large scale integrated CMOS-photonic chips.

We have previously proposed all-optical half-adder/subtractor, full-adder/subtractor and MUX/DEMUX at pump wavelength of 400 nm, using silicon MRRs in which the dynamics were analyzed based on a simple model of a 1 × 2 MRR configuration [27]. However, a more accurate analysis that incorporates scattering losses, linear and non-linear effects needs to be undertaken for a rigorous analysis of all-optical switching in add-drop silicon MRRs. Recently, we have proposed a theoretical model to analyze all-optical switching in silicon 2 × 2 MRRs and used it to design reversible Fredkin and

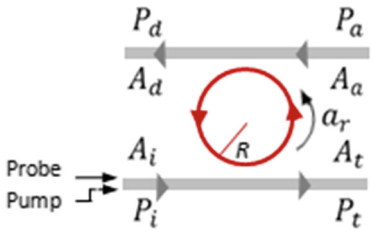

Fig. 1. Schematic of the All-Optical Silicon MRR Switch.

Toffoli logic gates, DEMUX/MUX, Reconfigurable Logic Unit, comparators and flip-flops [28, 29].

In this paper, we extend our previous work to design important all-optical ultrafast reversible Peres logic gate and Feynman-Double gate, based on all-optical switching by TPA induced free-carrier injection in silicon 2 × 2 MRRs. The circuits have been numerically simulated based on coupled-mode theory and switching has been optimized to realize low-power (25 mW) ultrafast (40 Gb/s) logic operations at communication wavelengths, i.e., 1550.7 and 1568.5 nm.

2 Theoretical Model

The switching response of the silicon add-drop MRR is modeled considering the propagation of pump and probe using time-domain coupled-mode theory, based on the theoretical model proposed earlier [29, 30]. Figure 1 shows the all-optical switch in a 2 × 2 add-drop silicon MRR where the input ports are P_i (input) and P_a (add) whereas the output ports are P_t (through) and P_d (drop) respectively. The ring is considered as a lumped oscillator, $A_x(x = i, a, t, d)$ is the field amplitude and $|A_x|^2(x = i, a, t, d)$ is the power of the waveguide mode and supports a travelling wave of amplitude $A_r(A_i \neq 0, A_a = 0)$, which is normalized so that $|A_r|^2$ represents the total power flowing through the cross-section A of the MRR at time t. The total energy stored in the ring is $|a_r|^2$ with energy amplitude a_r, which decays at the total rate $r = \tau^{-1} = r_o + r_e + r_d$. The probe is at high transmission at P_t of the MRR in the absence of the pump. When the pump is given, it generates free carriers inside the MRR due to TPA which reduces the refractive index of silicon through plasma-dispersion effect. This changes the resonance wavelength of the resonator, which couples the probe into the MRR, yielding a high transmission at P_d and low transmission at P_t.

To analyze the dynamic behavior of the switching mechanism for add-drop (1 × 2) geometry, the rate equations for the energy normalized pump and probe amplitudes a_r^{pump} and a_r^{probe} in the MRR are given by [29],

$$\frac{d}{dt}a_r^{pump}(t) = -j\left[\omega_{pump} - \omega_o - \Delta\omega_o^L(t) - \Delta\omega_o^{NL}(t)\right]a_r^{pump}(t) - \left[r_o + \Delta r_o^L(t) + \Delta r_o^{NL}(t)\right]a_r^{pump}(t) - (r_e + r_d)a_r^{pump}(t) - j\sqrt{2r_e}A_i^{pump}(t), \tag{1a}$$

$$\frac{d}{dt}a_r^{probe}(t) = -j\left[\omega_{pump} - \omega_o - \Delta\omega_o^L(t) - \Delta\omega_o^{NL}(t)\right]a_r^{probe}(t) - \left[r_o + \Delta r_o^L(t) + \Delta r_o^{NL}(t)\right]a_r^{probe}(t) - (r_e + r_d)a_r^{probe}(t) - j\sqrt{2r_e}A_i^{probe}(t). \tag{1b}$$

Here, r_o, r_e and r_d are the energy decay rates, ω_o is the resonance frequency, $\Delta\omega_o^L$ and $\Delta\omega_o^{NL}$ are the frequency shifts where as Δr_o^L and Δr_o^{NL} are the energy decay rates due to linear and non-linear effects respectively. The linear contribution to resonance frequency shift and energy decay rate are given by [29],

$$\Delta\omega_o{}^L = -\omega_o\Gamma\frac{\Delta n}{n_r} \quad \text{and} \quad \Delta r_o{}^L = \Gamma\frac{c\Delta\alpha}{2n_r} \tag{2}$$

Where n_r is the refractive index of ring waveguide core and Γ is confinement factor. The induced real refractive index and optical absorption coefficient variations (Δn and $\Delta\alpha$) at wavelength 1.55 μm are given by [30],

$$\Delta n = \Delta n_e + \Delta n_h = -\left[8.8 \times 10^{-22}\Delta N_e + 8.5 \times 10^{-18}(\Delta N_h)^{0.8}\right] \tag{3a}$$

$$\Delta\alpha = \Delta\alpha_e + \Delta\alpha_h = \left[8.5 \times 10^{-18}\Delta N_e + 6 \times 10^{-18}(\Delta N_h)\right] \tag{3b}$$

Δn_e and Δn_h are the refractive-index changes due to change in electron concentration $\Delta N_e(\text{cm}^{-3})$ and hole concentration $\Delta N_h(\text{cm}^{-3})$ respectively, where as $\Delta\alpha_e(\text{cm}^{-1})$ and $\Delta\alpha_h(\text{cm}^{-1})$ are absorption coefficient variations due to ΔN_e and ΔN_h respectively. The small nonlinear index and absorption changes due to Kerr effect are given by, $\Delta n^{NL} = n_{21}I_{pump}$ and $\Delta\alpha^{NL} = \beta I_{pump}$, where n_{21} and β are the Kerr and TPA coefficients respectively. The input pump intensity coupled into MRR is $I_{pump} = \frac{1}{2}c\varepsilon_o n\left|\overrightarrow{E_{pump}}\right|^2$. Assuming that refractive index of core is uniform, the nonlinear changes are [29],

$$\Delta\omega_o^{NL} = -\omega_o\frac{cn_{21}}{n_r^2}\frac{\left|a_r^{pump}\right|^2}{V_{eff}} \text{and } \Delta r_o^{NL} = \beta\frac{c^2}{2n_r^2}\frac{\left|a_r^{pump}\right|^2}{V_{eff}} \tag{4}$$

Here, $V_{eff} = LA_{eff}$, is the effective volume of the MRR and A_{eff} is the effective area. The output power of the probe then gets modulated by the resonance shift. After the pump leaves, the resonant wavelength and probe's transmission relaxes back due to fast recombination of the carriers determined by the carrier recombination lifetime. The red-shift caused by the Kerr effect is smaller than the blue-shift, due to which the latter effect dominates in silicon MRR. The output power of the probe then gets modulated by the resonance shift. In the present analysis, the nonlinear effects and free carriers are generated solely due to the pump and not due to the weaker probe. The free carrier concentration change ($\Delta N_e = \Delta N_h = \Delta N$) generated predominantly by TPA is given by $\frac{dN(t)}{dt} = \frac{\beta I_{pump}^2}{2h\nu} - \frac{N(t)}{\tau_{fc}}$, which can also be written as [29],

$$\frac{dN(t)}{dt} = \frac{\Delta r_o^{NL}}{\hbar\omega_{pump}} \frac{\left|a_r^{pump}\right|^2}{V} - \frac{N(t)}{\tau_{fc}} \tag{5}$$

where, $\hbar\omega_{pump}$ is the pump photon energy and τ_{fc} is the free carrier recombination lifetime.

The transmitted probe amplitudes at P_t and P_d are given by:

$$A_{Through}^{probe}(t) = A_i^{probe}(t) - j\sqrt{2r_e}a_r^{probe}(t), \tag{6a}$$

$$A_{Drop}^{probe}(t) = -j\sqrt{2r_d}a_r^{probe}(t) \tag{6b}$$

The transmission response of the MRR at P_t and P_d respectively is given by,

$$T(\omega) = \frac{A_t}{A_i} = \frac{j(\omega-\omega_o)+r-2r_e}{j(\omega-\omega_o)+r}, D(\omega) = \frac{A_d}{A_i} = \frac{-2\sqrt{r_e r_d}}{j(\omega-\omega_o)+r} \tag{7}$$

To calculate the complex resonance frequency and the transient response, (1a, 1b) is numerically integrated using (2)–(5). The transmitted probe amplitudes at P_t and P_d can be evaluated by using (6a, 6b) and the corresponding normalized power transmission (NPT) can be plotted using (7).

3 Results and Discussion

The basic switching configuration in Fig. 1 has been used to design various computing circuits. The temporal response for the proposed computing circuits has been simulated by considering the experimental conditions and parameters. The optical switching characteristics, i.e. the variation in NPT with time for the probe have been analyzed by solving Eqs. (1a, 1b)–(7) through computer simulations. To design the proposed reversible logic gates, we consider a silicon 2 × 2 MRR optimally coupled to the waveguides and the experimental values listed in Table 1 from several experiments to achieve low-power, ultrafast and high contrast switching [22, 23, 30, 31]. Switching time depends on the ring photon lifetime and the recombination time of the induced carriers. However, the carrier lifetime is generally longer than the cavity photon lifetime. To increase bit rate and speed of operation, the free-carrier lifetime can be significantly reduced by a combination of distinct mechanisms such as, shrinking the cavity size, oxygen or ion implantation etc. [31, 32].

Without the pump, $\lambda_{probe} = 1568.55$ nm has high transmission at P_t and low transmission at P_d. When the pump is on, there is increase in normalized transmission at P_t and a complementary decrease at P_d. Considering the coupling conditions, the computed values of power coupling coefficients $(\kappa_e = \kappa_d)$ is $\cong 0.2$. The average input control power P_c is calculated to be $\sim$25 mW and pulse energy $E_{pump} \sim 2.6$ pJ. To estimate practical power values, we consider the experimental conditions of Xu *et al.* with a probe laser of 5 mW, of which $\sim$30 % (1.5 mW) gets coupled through a nano-tapered waveguide [22]. At off-resonance $\sim$92 % (1.4 mW) and at resonance

only ~15 % (0.2 mW) of it gets coupled from P_i to P_t or from P_a to P_d [24]. We consider positive logic and an upper limit of low-state output power P_{OL} = 0.3 mW (maximum value for logic 0) and minimum threshold for high-state output power P_{OH} = 0.9 mW (minimum value for logic 1) for probe output, to realize various logic operations. We assume 18 % of the pump (~ 8 dB loss due to coupling, scattering and absorption losses) i.e. ~4.5 mW is detected from the MRR [35]. Considering the all-optical silicon MRR switch (Fig. 1) as a template for designing higher computing circuits using pump and probe intensities as the inputs, the NPT with time has been simulated by solving Eqs. (1a, 1b)–(7) using the experimental parameters listed in Table 1.

Table 1. Parameters used in the simulations [22, 23, 30, 31]

Radius (R)	5 μm
Rectangular cross-section (A)	450x250 nm
$\lambda_{pump}(\lambda_{res1})$	1550.55 nm
$Q_{res1}(\lambda_{res1}/\Delta\lambda_{FWHM1})$	11076
$\Delta\lambda_{FWHM1}$	0.14 nm
$\tau_{cav1}\left(\lambda_{res1}^2/2\pi c\Delta\lambda_{FWHM1}\right)$	9.1 ps
$\lambda_{probe}(\lambda_{res2})$	1568.55 nm
$Q_{res2}(\lambda_{res2}/\Delta\lambda_{FWHM2})$	9804
$\Delta\lambda_{FWHM2}$	0.16 nm
$\tau_{cav2}\left(\lambda_{res2}^2/2\pi c\Delta\lambda_{FWHM2}\right)$	8.1 ps
Free-carrier lifetime (τ_{fc})	15 ps
Pump pulse width	0.1 ps
Probe pulse width	18 ps
Pump-probe delay	6 ps
$P_c(E_{pump})$	~25 mW (~2.6 pJ)
FSR $= \lambda_O^2/Ln_g$	18 nm
Group index (n_g)	4.35
Γ	0.92
n_r	3.48
A/A_{eff}	0.82
B	0.79 cm/GW
n_{21}	$0.45\text{x}10^{-13}$ cm^2/W

TPA at higher powers leads to thermo-optic effect that has not been considered in the present analysis. However, it can be resolved either by athermalizing silicon MRRs by considerably decreasing the temperature-dependence using negative thermo-optic materials/interferometric structures or by using integrated heaters [33, 34]. Another alternative could be employing strain in the silicon waveguide by controlling the overcladding deposition conditions. Strain reduces the refractive index with temperature, which counterbalances the thermo-optic effect.

3.1 Reversible Peres Logic Gate

The Peres gate is a reversible 3 × 3 logic gate, where one output is the same as one input (O_1), the second output is XOR of the first two inputs (O_2) and the third output is XOR of the AND of first two inputs (O_3), as shown in Fig. 2(a). The design of an all-optical Peres gate with silicon MRRs is shown schematically in Fig. 2(b) with the pump I_1 and the two probe signals I_2 and I_3 to result in the desired operation as shown in Table 2. Figure 2 (c) shows the simulated response of the proposed gate.

The Peres gate requires 2 MRRs for its realization. MRR M_1 is an all-pass ring resonator and the time-domain coupled-mode theory [30] has been used to obtain the response at its through port. Initially, when pump I_1 is off, the probe I_3 is obtained at the output port P_t. The short pump pulse I_1 creates electron-hole pairs in the silicon MRR due to two-photon absorption (TPA). According to Drude's model, the refraction and absorption due to free carriers is given by $\Delta n = -(e^2\lambda^2/8\pi^2 c^2_{\varepsilon_o} n)[\Delta N_e/m_{ce} + \Delta N_h/m_{ch}]$ and $\Delta\alpha = -(e^3\lambda^2/4\pi^2 c^3_{\varepsilon_o} n)[\Delta N_e/m^2_{ce}\mu_e + \Delta N_h m_{ch}/m^2_{ch}\mu_h]$, where e is the electronic charge, ε_o is the permittivity of free space, m_{ce} is the conductivity of effective mass of electron, m_{ch} is the conductively of effective mass of the holes, μ_e is electron mobility and μ_h is hole mobility [36]. The generated carriers shift the resonance frequency of the ring by reducing the refractive index ($n = n_o + ik$ where the imaginary part of the refractive index depends on the absorption α, $\alpha = 4\pi k/\lambda$) and thus changes the transmission of the probe which now couples to yield a high transmission at P_d and low transmission at P_t. For M_2, in the absence of the pump I_1, I_2 propagates to P_t and $\overline{I_2}$ is obtained at P_d. However, when I_1 is given, the resonance wavelength shifts due to plasma-dispersion effect, tuning the resonator due to which the probe I_2 now couples into the MRR resulting in an increase in transmission at P_d. Similarly $\overline{I_2}$ is now switched to P_t.

Case (i): Initially, when none of the inputs are applied, all output ports are low. Case (ii): When $I_1 = I_2 = 0$ and $I_3 = 1, O_2$ is low and I_3 couples to O_3, resulting in $O_3 = 1$, corresponding to the simulated NPT ~92 % at 100 ps as shown in Fig. 2(c–v). Case (iii): When $I_1 = 0$, $I_2 = 1$ and $I_3 = 0, I_2$ couples to O_2 ($O_2 = 1$, corresponding to the simulated NPT at 200 ps in Fig. 2 (c–iv)) and O_3 is low. Case (iv): When $I_1 = 0$, $I_2 = 1$ and $I_3 = 1, O_2$ and O_3 are both high as I_2 and I_3 get directly transmitted to these ports, without getting switched by M_1 or M_2 (simulated NPT at 290 ps). Case (v): When $I_1 = 1$ and $I_2 = I_3 = 0$, $\overline{I_2}$ is high which gets switched to O_2 (simulated NPT at 380 ps). Case (vi): When $I_1 = 1, I_2 = 0$ and $I_3 = 1$, again O_2 is high due to switching of $\overline{I_2}$ (NPT at 475 ps), whereas now, I_3 gets switched by M_1 making $O_3 = 0$. Case (vii): When $I_1 = I_2 = 1$ and $I_3 = 0, I_2$ gets switched by M_2, leading to $O_2 = O_3 = 0$. Case (viii): When $I_1 = I_2 = I_3 = 1$, I_2 and I_3 get switched by M_2 and M_1 respectively to result in O_2 and $O_3 = 0$. Reversible logic gates can be used to design various computing circuits that include demultiplexer/multiplexer, programmable logic array, arithmetic logic unit, counters etc. [37, 38]. For instance, using two Peres gates, a binary full-adder can also be realized.

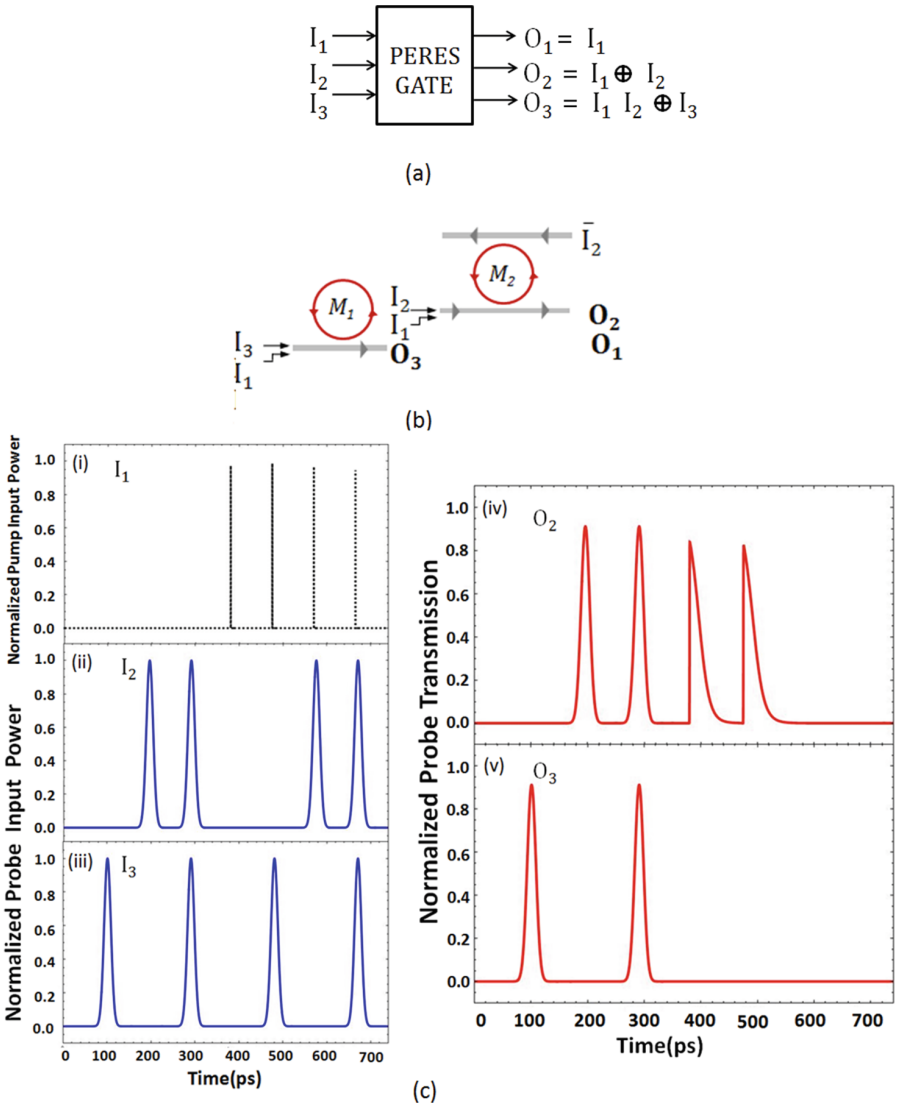

Fig. 2. All-optical reversible Peres Logic gate, (a) Block diagram, (b) Schematic using silicon ring resonators, (c) Temporal response: (i) Pump input I_1 (dashed), (ii) Probe input I_2 (solid), (iii) Probe input I_3 (solid), (iv) Probe Output O_2, and (v) Probe Output O_3.

3.2 Reversible Feynman-Double Gate

The Feynman-Double gate is another 3 × 3 reversible gate which maps one input to one output, while the second output is the XOR of the first two inputs and the third output is the XOR of the second and third inputs, as shown in the block diagram in Fig. 3(a).

Table 2. Truth Table of all-optical Peres logic gate

Pump Input (mW)	Probe Input (mW)		Outputs (mW)		
I_1	I_2	I_3	O_1	O_2	O_3
0	0	0	0	0	0
0	0	1 (1.5)	0	0 (0.3)	1 (1.4)
0	1 (1.5)	0	0	1 (1.4)	0 (0.3)
0	1 (1.5)	1 (1.5)	0	1 (1.4)	1 (1.4)
1 (25)	0	0	1 (4.5)	1 (1.3)	0 (0.2)
1 (25)	0	1 (1.5)	1 (4.5)	1 (1.2)	0 (0.2)
1 (25)	1 (1.5)	0	1 (4.5)	0 (0.2)	0 (0.2)
1 (25)	1 (1.5)	1 (1.5)	1 (4.5)	0 (0.2)	0 (0.2)

The design based on two optically controlled silicon ring resonators is shown in Fig. 3 (b). The input control signal I_1 directly maps out to output O_1, satisfying the first requirement. The probe inputs I_2 and I_3 form the other two inputs, with outputs at O_2 and O_3. We consider the various combinations of the pump and probe inputs resulting in respective outputs as described in Table 3.

For the case of the Feynman-Double gate both the MRRs are add-drop MRRs. With pump I_1 off, the probe I_2 is transmitted directly to the output port P_t and $\overline{I_2}$ is directly transmitted to P_d. When the pump I_1 hits the MRR, free carriers are generated within the MRR due to which I_2 now couples to yield a high transmission at P_d and low transmission at P_t. Similarly I_2 is now obtained at P_t. As the free carriers recombine, the resonance of the ring is restored to its original value. For M_2, in the absence of the pump I_1, I_3 propagates to P_t and $\overline{I_2}$ propagates to P_d. However, when I_1 is given, the resonance wavelength shifts, tuning the resonator due to which the probe, I_3 now couples into the MRR resulting in an increase in transmission at P_d whereas $\overline{I_3}$ switches to P_t.

Case (i): When none of the inputs are applied, no output is obtained. Case (ii): When $I_1 = I_2 = 0$ and $I_3 = 1, I_3$ passes over to O_3, resulting in $O_3 = 1$, corresponding to the simulated NPT $\sim$92 % at 100 ps as shown in Fig. 3(c–v). $\overline{I_2} = 1$ does not get switched resulting in $O_2 = 0$. Case (iii): When $I_1 = 0, I_2 = 1$ and $I_3 = 0$, I_2 passes over to O_2 ($O_2 = 1$, corresponding to the simulated NPT at 200 ps in Fig. 3 (c–iv)) and I_3 ensures that O_3 is low. Case (iv): When $I_1 = 0, I_2 = I_3 = 1, O_2 = O_3 = 1$ (simulated NPT at 290 ps) as both MRRs are in the off-resonant state. Case (v): When $I_1 = 1, I_2 = I_3 = 0$, and $\overline{I_2} = \overline{I_3} = 1$, get switched as both MRRs are in on-resonant state to make $O_2 = O_3 = 1$ (simulated NPT at 380 ps). Case (vi): When $I_1 = 1, I_2 = 0$ and $I_3 = 1$, $\overline{I_2}$ is high which is routed to O_2, ($O_2 = 1$, NPT at 475 ps) while I_3 gets switched to emerge at Drop port of M_2 to result in a low output at O_3. Case (vii): When $I_1 = I_2 = 1$ and $I_3 = 0, I_2$ gets switched to result in $O_2 = 0$ and $\overline{I_3}$ gets switched to result in $O_3 = 1$ (corresponding to the simulated NPT at 570 ps). Case (viii): When $I_1 = I_2 = I_3 = 1, I_2$ and I_3 get switched to result in low outputs at O_2 and O_3. The above combinations result in the circuit in Fig. 3 that implements Feynman-Double gate logic as shown in Truth Table 3.

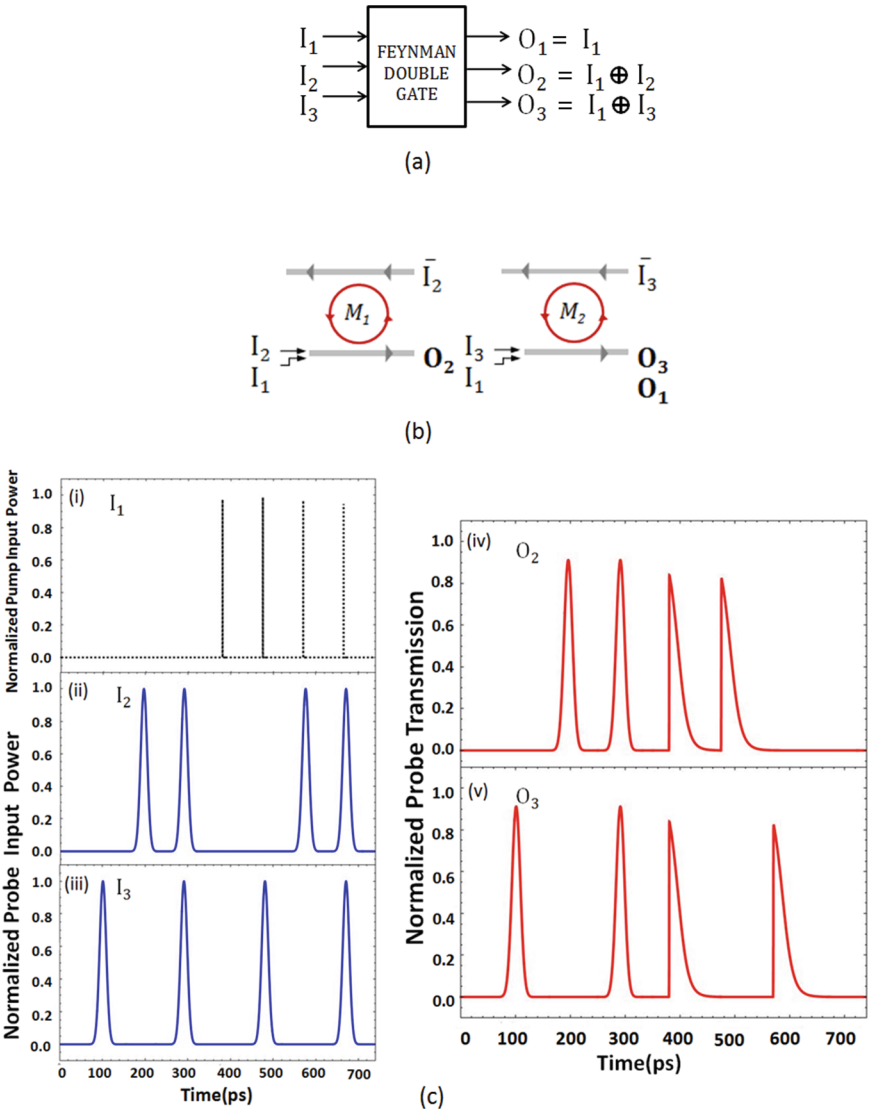

Fig. 3. All-optical reversible Feynman-Double Logic gate, (a) Block diagram, (b) Schematic using silicon ring resonators, (c) Temporal response: (i) Pump input I_1 (dashed), (ii) Probe input I_2 (solid), (iii) Probe input I_3 (solid), (iv) Probe Output O_2, and (v) Probe Output O_3.

In our previous work, we have presented designs of all-optical Boolean as well as conservative and reversible logic gates with optically controlled microresonators [37, 38]. Higher computing circuits such as half/full adder-subtractor, multiplexer/de-multiplexer, and arithmetic logic unit circuits have also been designed using all-optical switching in the photochromic bacteriorhodopsin protein-coated silica microcavities in contact between two tapered single-mode fibers at telecom wavelengths [39, 40].

Table 3. Truth table of all-optical Feynman-Double logic gate

Pump Input (mW)	Probe Input (mW)		Outputs (mW)		
I_1	I_2	I_3	O_1	O_2	O_3
0	0	0	0	0	0
0	0	1 (1.5)	0	0 (0.3)	1 (1.4)
0	1 (1.5)	0	0	1 (1.4)	0 (0.3)
0	1 (1.5)	1 (1.5)	0	1 (1.4)	1 (1.4)
1 (25)	0	0	1 (4.5)	1 (1.3)	1 (1.3)
1 (25)	0	1 (1.5)	1 (4.5)	1 (1.3)	0 (0.2)
1 (25)	1 (1.5)	0	1 (4.5)	0 (0.2)	1 (1.3)
1 (25)	1 (1.5)	1 (1.5)	1 (4.5)	0 (0.2)	0 (0.2)

Although low-power control signals (<200 μW) were used, the speed of operation is ∼μs that is governed by the trans-cis isomerization of the photosensitive protein. It is important to achieve low-power as well as high switching speed to realize high bit rates, for practical applications.

All-optical switching in silicon MRRs is based on the nonlinear intensity-dependent refractive index and hence is sensitive to pump and probe intensities. The non-linear refractive index and absorption changes induce a shift in the resonant wavelength due to the generation of free carriers. In the proposed model, the pump and probe wavelengths can be interchanged as shown experimentally [22, 23]. In the theoretical model, it is assumed that the free carriers and nonlinear effects are generated only by the pump since the probe is much weaker. However, if the probe is at a relatively higher intensity, it will affect the switching results.

In the proposed designs, we have considered the experimental conditions of Xu *et al.* [22] with probe power of 1.5 mW (after coupling) and the pump power ∼25 mW. The theoretical simulations of all-optical switching in silicon all-pass (1 × 1) and add-drop (1 × 2) MRRs are in good agreement with reported experimental results. We can give multiple pump inputs to the MRR, in a way that the combined pump intensities result in 85–90 % modulation. For example, Xu and Lipson [23] have shown an all-optical AND/NAND gate with two pumps of ∼2mW each and one probe beam using a single 1 × 1 MRR with 85 % modulation. Similarly, multiple probe inputs can also be given simultaneously, so that the combined probe intensities are less than the pump intensity required for considerable modulation (say 30 %). For instance, in a 5 μm MRR, Q ∼ 4000 at $\lambda_{pump} = 1558.6$ nm, as long as the combined probe intensities are <2 pJ, there will be no considerable effect on switching as can be seen in Table 4. Thus, in the present proposed circuits, considering the threshold probe power ∼15 mW (∼30 % modulation), as many as 30 probe inputs can be injected into the MRR, considering input probe power ∼0.5 mW (after coupling).

Simultaneously input of probes at the add and drop ports, may induce intraband crosstalk in the MRR which increases as the frequency difference between the two signals increases [41] Coherent input signals from the same laser source at both the ports can be given simultaneously to avoid any frequency mismatch. Crosstalk can also be minimized by using a high coupling strength $(\kappa_e = \kappa_d \cong 0.85)$, an active ring

Table 4. The effect of E_{pump} on change in free carriers, refractive index, resonant wavelength and switching contrast

E_{pump}(pJ)	ΔN (cm^{-3})	Δn	$\Delta\lambda_o$(nm)	Switching Contrast (%)
3	1.04×10^{17}	-4×10^{-4}	−0.176	88
2.5	5.1×10^{16}	-2×10^{-4}	−0.088	50
2	2.0×10^{16}	-1×10^{-4}	−0.038	30
1	1.4×10^{15}	-1×10^{-5}	−0.004	2

resonator or alternatively designing the circuits with a single MRR replaced by a double-stage configuration [41].

Wavelength division multiplexing (WDM) in silicon MRRs has been shown to switch a large number (n ∼ 40) of wavelength channels spaced by ∼0.85 nm (crosstalk ∼15 dB, insertion loss <3 dB) [25]. Considering WDM inputs are given simultaneously, then 20 (power penalty: 1 dB (through port), 2.3 dB (drop port)) wavelength channels can be given in a 1 × 2 silicon MRR [Lee *et al.* (2008)]. MRR switch can be used to simultaneously switch on and off a large number of wavelength channels due to its relatively small Free Spectral Range (FSR) [42].

The pump-probe technique can be used advantageously to cascade the gates to realize higher arithmetic and logic circuits. Complex circuits can be realized using these reversible logic gates. For instance, all-optical Fredkin logic gate has been used to realize all-optical full-adder, MUX/DEMUX, XOR/XNOR with bacteriorhodopsin protein coated silica microcavities by cascading the pump and the probe outputs at P_t and P_d as inputs to other logic gates [37]. Similarly Peres gate can also be used to realize a binary full-adder.

The 2 × 2 silicon MRR configuration is extremely versatile and can be used to design any desired logic circuit. To design a given logic function, the required number of logical inputs/outputs have to be realized with multiple probe and pump signals and the number of switches. A single MRR can have 3 inputs and 3 outputs that can be used to realize the Fredkin and Feynman gates. However, Toffoli, Peres and Feynman Double gates require 2 MRRs. The design considerations for various logic circuits proposed in literature are shown in Table 5.

Complex reversible circuits based on reversible logic gates, memory elements such as RAM, counters, registers etc. can be designed using a similar configuration. It would be interesting to investigate these designs at lower intensities using more compact geometries i.e., photonic crystal cavities [43] and nanoring resonators [44]. Graphene based ring modulators can also be explored to design computing circuits as they have higher electron mobility and can be modulated directly using loss modulation rather than on loss-induced refractive index variations [45].

Since in the present designs, the state of each switch is controlled by an input logic signal rather than the output of previous switches, all switches operate simultaneously and the switching time does not accumulate. The proposed designs are general, use minimal switches and inputs, and can be implemented in both fiber-optic and integrated optic formats. The pump-probe technique can be used advantageously to achieve

Table 5. Design considerations for various logic circuits

Logic Gates/Circuits	Number of MRRs	Configuration	Maximum number of inputs	Maximum number of outputs
AND/NAND [23]	1	All-pass	3	3
Fredkin gate [28]	1	Add-drop	4	4
Feynman gate				
XOR/XNOR				
S-R Flip-flops [29]				
D Flip-flops [29]				
Encoder	2	Add-drop	7	7
Decoder				
Toffoli gate [28]				
Feynman Double gate				
Peres Gate				
Half-Adder/ Subtractor				
T Flip-flop [29]				
Comparator [29]				
Multiplexer/ Demultiplexer [28]	3	Add-drop	10	10
Full-Adder/ Subtractor	4	Add-drop	13	13
Reconfigurable Logic Unit [29]	6	Add-drop	19	19
TSG gate				

cascadibility. In our simulations, a pump-probe delay of 6 ps has been considered i.e., the pump is incident 6 ps before the probe peak to achieve a high switching contrast (85 %). The present designs based on experimental conditions have a single MRR device of $\sim$132 μm^2 footprint with switching time $\sim$25 ps. The control and probe signals are both considered as logical inputs instead of only control signals. This results in lesser number of switches and inputs to the circuit and leads to lower delays and higher bit rates.

4 Conclusion

We have presented designs of all-optical ultrafast reversible Peres logic gate and Feynman-Double logic gate using an accurate theoretical model based on time-domain coupled-mode theory. All-optical switching in add-drop silicon MRRs modulated using TPA-induced carrier injection leads to ultrafast switching (25 ps), low-power operation (25 mW) and high modulation depth (85 %), enabling logic operations at 40 Gb/s. Advantages of DL, high Q-factor, tunability, high fan-out, reconfigurability, reversibility,

scalability, simplicity and flexibility of cascading switches in 2D architectures to form circuits make the designs favorable for practical applications. The designs are general and can be implemented with any other externally controlled microresonator switch.

Acknowledgment. P. S. is grateful to the University Grants Commission, Government of India for the award of UGC-BSR fellowship.

References

1. Priolo, F., Gregorkiewicz, T., Galli, M., Krauss, T.F.: Silicon nanostructures for photonics and photovoltaics. Nat. Nanotech. **9**, 19–32 (2014)
2. Jalali, B., Fathpour, S.: Silicon photonics. IEEE J. Lightwave Technol. **24**, 4600–4615 (2006)
3. Reed, G.T., Mashanovich, G., Gardes, F.Y., Thomson, D.J.: Silicon optical modulators. Nat. Photon. **4**, 518–526 (2010)
4. Moss, D.J., Morandotti, R., Gaeta, A.L., Lipson, M.: New CMOS-compatible platforms based on silicon nitride and Hydex for nonlinear optics. Nat. Photon. **7**, 597–607 (2013)
5. Heck, M.J.R., Bauters, J.F., Davenport, M.L., Doylend, J.K., Jain, S., Kurczveil, G., Srinivasan, S., Tang, Y., Bowers, J.E.: Hybrid silicon photonic integrated circuit technology. IEEE J. Sel. Top. Quant. Electron. **19**, 6100117–6100134 (2012)
6. Xu, Q., Soref, R.: Reconfigurable optical directed-logic circuits using microresonator-based optical switches. Opt. Exp. **19**, 5244–5259 (2011)
7. Zhang, L., Ding, J., Tian, Y., Ji, R., Yang, L., Chen, H., Zhou, P., Lu, Y., Zhu, W., Min, R.: Electro-optic directed logic circuit based on microring resonators for XOR/XNOR operations. Opt. Exp. **20**, 11605–11614 (2012)
8. Tian, Y.H., Zhang, L., Ji, R.Q., Yang, L., Zhou, P., Chen, H.T., Ding, J.F., Zhu, W.W., Lu, Y.Y., Jia, L.X., Fang, Q., Yu, M.B.: Proof of concept of directed OR/NOR and AND/NAND logic circuit consisting of two parallel microring resonators. Opt. Lett. **36**, 1650–1652 (2011)
9. Lin, S., Ishikawa, Y., Wada, K.: Demonstration of optical computing logics based on binary decision diagram. Opt. Exp. **20**, 1378–1384 (2012)
10. Landauer, R.: Irreversibility and heat generation in the computing process. IBM J. Res. Dev. **5**, 183–191 (1961)
11. Bennett, C.H.: Logical reversibility of computation. IBM J. Res. Dev. **17**, 525–532 (1973)
12. Maruyama, K., Nori, F., Vedral, V.: The physics of Maxwell's demon and information. Rev. Mod. Phys. **81**, 1–22 (2009)
13. Peres, A.: Reversible logic and quantum computers. Phys. Rev. A **32**, 3266–3276 (1985)
14. Fredkin, E., Toffoli, T.: Conservative logic. Int. J. Theor. Phys. **21**(3–4), 219–253 (1982)
15. Huang, Y.-P., Kumar, P.: Interaction-free quantum optical Fredkin gates in χ^2 microdisks. IEEE J. Quantum Electron. **18**, 600–611 (2012)
16. Fedorov, A., Steffen, L., Baur, M., Silva, M.P., Wallraff, A.: Implementation of a Toffoli gate with superconducting circuits. Nature **481**, 170–172 (2011)
17. Thapliyal, H., Ranganathan, N.: Design of reversible sequential circuits optimizing quantum cost, delay, and garbage outputs. ACM J. Emerg. Technol. Comput. Syst. (JETC) **6**, 14–31 (2010)
18. Thapliyal, H., Ranganathan, N.: Reversible logic-based concurrently testable latches for molecular qca. IEEE Trans. Nanotechnol. **9**, 62–69 (2010)

19. Lipson, M.: Guiding, modulating, and emitting light on silicon-challenges and opportunities. J. Lightwave Technol. **23**, 4222–4238 (2005)
20. Bogaerts, W., De Heyn, P., Van Vaerenbergh, T., De Vos, K., Selvaraja, S.K., Claes, T., Dumon, P., Bienstman, P., Van Thourhout, D., Baets, R.: Silicon microring resonators. Laser Photon. Rev. **6**, 47–73 (2012)
21. Almeida, V.R., Barrios, C.A., Panepucci, R.R., Lipson, M.: All-optical control of light on a silicon chip. Nature **431**, 1081–1084 (2004)
22. Xu, Q., Schmidt, B., Pradhan, S., Lipson, M.: Micrometre-scale silicon electro-optic modulator. Nature **435**, 325–327 (2005)
23. Xu, Q., Lipson, M.: All-optical logic based on silicon micro-ring resonators. Opt. Exp. **15**, 924–929 (2007)
24. Preble, S.F., Xu, Q., Lipson, M.: Changing the color of light in a silicon resonator. Nat. Photon. **1**, 293–296 (2007)
25. Dong, P., Preble, S.F., Lipson, M.: All-optical compact silicon comb switch. Opt. Exp. **15**, 9600–9605 (2007)
26. Caulfield, H.J., Soref, R.A.: Universal reconfigurable optical logic with silicon-on-insulator resonant structures. Photonics Nanostruct. **5**, 14–20 (2007)
27. Sethi, P., Roy, S.: All-optical ultrafast adder/subtractor and MUX/DEMUX circuits with silicon microring resonators. In: Dolev, S., Oltean, M. (eds.) OSC 2012. LNCS, vol. 7715, pp. 42–53. Springer, Heidelberg (2013)
28. Sethi, P., Roy, S.: All-optical ultrafast switching in 2 × 2 silicon microring resonators and its application to reconfigurable DEMUX/MUX and reversible logic gates. IEEE J. Lightw. Technol. **32**, 2173–2180 (2014)
29. Sethi, P., Roy, S.: Ultrafast all-optical flip-flops, simultaneous comparator-decoder and reconfigurable logic unit with silicon microring resonator switches. IEEE J. Sel. Top. Quantum. Electron. **20**, 118–125 (2014)
30. Manolatou, C., Lipson, M.: All-optical silicon modulators based on carrier injection by two-photon absorption. IEEE J. Lightwave Technol. **24**, 1433–1439 (2006)
31. Waldow, M., Plötzing, T., Gottheil, M., Först, M., Bolten, J., Wahlbrink, T., Kurz, H.: 25 ps all-optical switching in oxygen implanted silicon-on-insulator microring resonator. Opt. Exp. **16**, 7693–7702 (2008)
32. Chin, A., Lee, K.Y., Lin, B.C., Horng, S.: Picosecond photoresponse of carriers in Si ion-implanted Si. Appl. Phys. Lett. **69**, 653–655 (1996)
33. Guha, B., Kyotoku, B.B.C., Lipson, M.: CMOS-compatible athermal silicon microring resonators. Opt. Exp. **18**, 3487–3493 (2010)
34. Padmaraju, K., Chan, J., Chen, L., Lipson, M., Bergman, K.: Thermal stabilization of a microring modulator using feedback control. Opt. Exp. **20**, 27999–28008 (2012)
35. Turner, A.C., Foster, M.A., Gaeta, A.L., Lipson, M.: Ultra-low power parametric frequency conversion in a silicon microring resonator. Opt. Exp. **16**, 4881–4887 (2008)
36. Soref, R.A., Bennett, B.R.: Electrooptical effects in silicon. IEEE J. Quant. Electron. **23**, 123–129 (1987)
37. Roy, S., Prasad, M.: Novel proposal for all-optical Fredkin logic gate with bacteriorhodopsin-coated microcavity and its applications. Opt. Eng. **49**, 065201–065210 (2010)
38. Roy, S., Sethi, P., Topolancik, J., Vollmer, F.: All-optical reversible logic gates with optically controlled bacteriorhodopsin protein-coated microresonators. Adv. Opt. Technol. **2012**, 727206–727212 (2012)
39. Roy, S., Prasad, M., Topolancik, T., Vollmer, F.: All-optical switching with bacteriorhodopsin protein coated microcavities and its application to low power computing circuits. J. Appl. Phys. **107**, 053115–053124 (2010)

40. Roy, S., Prasad, M.: Design of all-optical reconfigurable logic unit with bacteriorhodopsin protein coated microcavity switches. IEEE Trans. Nanobiosci. **10**, 160–171 (2011)
41. Simos, H., Mesaritakis, C., Alexandropoulos, D., Syvridis, D.: Dynamic analysis of crosstalk performance in microring-based add/drop filters. IEEE J. Lightw. Technol. **27**, 2027–2034 (2009)
42. Lee, B.G., Biberman, A., Dong, P., Lipson, M., Bergman, K.: All-optical comb switch for multiwavelength message routing in silicon photonic networks. IEEE Photon. Technol. Lett. **20**, 767–769 (2008)
43. Nozaki, K., Tanabe, T., Shinya, A., Matsuo, S., Sato, T., Taniyama, H., Notomi, M.: Sub-femtojoule all-optical switching using a photonic-crystal nanocavity. Nat. Photonics **4**, 477–483 (2010)
44. Sederberg, S., Driedger, D., Nielsen, M., Elezzabi, A.Y.: Ultrafast all-optical switching in a silicon-based plasmonic nanoring resonator. Opt. Exp. **19**, 23494–23503 (2011)
45. Midrio, M., Boscolo, S., Moresco, M., Romagnoli, M., Angelis, C.D., Locatelli, A., Capobianco, A.D.: Graphene–assisted critically–coupled optical ring modulator. Opt. Exp. **20**, 23144–23155 (2012)

http://www.springer.com/978-3-662-45710-8

Transactions on Computational Science XXIV
Special Issue on Reversible Computing
Gavrilova, M.L.; Tan, C.J.K.; Thapliyal, H.; Ranganathan, N. (Eds.)
2014, XIII, 147 p. 72 illus., Softcover
ISBN: 978-3-662-45710-8